Effects of the fringe field of Rayleigh-Taylor instability in the equatorial E and valley regions

E. Alam Kherani, Eurico R. de Paula, and Fernando C. P. Bertoni

Instituto Nacional de Pesquisas Espaciais, São José dos Campos, São Paulo, Brazil

[1]   We present a unified algorithm for the collisional interchange instabilities (Rayleigh-Taylor and gradient drift instabilities) occurring in the F and E regions of the equatorial ionosphere. The similar underlying mechanism of both instabilities enables us to derive the general two-dimensional continuity and potential equations. The equations are integrated numerically to study the nonlinear evolution of the polarization field (fringe field) associated with the generalized Rayleigh-Taylor instability. In particular, the effects of the fringe field into the equatorial E and transition (or valley) regions are investigated. The characteristics of the fringe field beneath the F region are investigated quantitatively for the first time. It is shown that the fringe field is capable of transporting plasma from the region where ions are highly magnetized (i.e., from the valley region). It is further shown that only under strongly driven but realistic conditions, the fringe field recognizes the part of the E region plasma where ions are marginally magnetized. The E region irregularities which are often located in such a region (near 120 km) during evening and nighttime can be effectively convected by the fringe field across the valley region and to the higher altitudes. On the other hand, because of the small ratio of ion-gyro-frequency to collision frequency below $120-115$ km altitude the fringe field is unable to convect the E region irregularities lying below this region. These characteristics are important in the context of observed valley region echoes which are yet to be explained quantitatively.   INDEX TERMS: 2415 Ionosphere: Equatorial ionosphere; 2471 Ionosphere: Plasma waves and instabilities; 2439 Ionosphere: Ionospheric irregularities; 2437 Ionosphere: Ionospheric dynamics; 2419 Ionosphere: Ion chemistry and composition (0335); KEYWORDS: Rayleigh-Taylor instability, fringe field, valley region, Crank-Nicholson implicit scheme, Pedersen conductivity, marginally magnetized

1.   Introduction

[2]   The generalized collisional Rayleigh-Taylor instability (GRT) plays a crucial role in the onset and development of equatorial spread F (ESF) turbulence [Haerendel, 1973]. Radar observations of ESF reveal the existence of rising plumes [Kelley et al., 1981]. These plumes are identified as large-scale depletions or bubbles and are believed to be generated by GRT. Numerous theoretical studies and numerical simulations of GRT [Scannepieco and Ossakow, 1976; Zargham and Seyler, 1987; Raghavarao et al., 1992; Huang et al., 1993] are performed to study the nonlinear evolution of large-scale ESF bubbles.

[3]   On occasion, the radar observations reveal the presence of valley and upper E region echoes during the occurrence of highly extended spread F plumes [Woodman and La Hoz, 1976; Hysell et al., 1990; Woodman and Chau, 2001]. These echoes are believed to be generated by the polarization field (fringe field) associated with the bubbles [Woodman and Chau, 2001]. In their numerical simulation of GRT, Alam

Kherani et al. [2002] have argued for the fringe field to be the potential cause of such echoes or irregular structures. The study was, however, restricted to the F region and did not explicitly include the electrodynamics beneath the F region. However, in order to know the complete ability of the fringe field to produce such structures, the inclusion of E and valley region dynamics is desired.

[4]   In the present investigation we derive the general continuity and potential equations for collisional interchange instability (CII), which include the dynamics of E, valley, and F regions. Instead of using the flux-corrected transport algorithm [Zalesak, 1979; Ossakow et al., 1979; Zalesak and Ossakow, 1980], the Crank-Nicholson implicit scheme is adopted for the time integration of the continuity equation. Recently, Huba et al. [2000] have used this scheme for their ambient ionospheric model Sami2 is Another Model of the Ionosphere (SAMI2).

2.   Model Equations and Algorithm

[5]   We adopt the following set of equations to study the collisional interchange instabilities in the equatorial F and E regions:

$$\frac{\partial n}{\partial t} + \nabla \cdot (n\mathbf{v}_e) = -\beta n - \alpha n^2 \tag{1}$$

$$\nabla \cdot \mathbf{J} = e\nabla \cdot [n(\mathbf{v}_i - \mathbf{v}_e)] = 0 \tag{2}$$

$$\mathbf{v}_{i,e} = \frac{\kappa_{i,e}}{1 + \kappa_{i,e}^2}\left(\frac{-c_{si,e}^2}{\nu_{i,en}}\nabla \log n + \frac{\mathbf{g}}{\nu_{i,en}} + b_{i,e}\mathbf{E}\right) \times \hat{b}$$
$$+ \frac{1}{1 + \kappa_{i,e}^2}\left(\frac{-c_{si,e}^2}{\nu_{i,en}}\nabla \log n + \frac{\mathbf{g}}{\nu_{i,en}} + b_{i,e}\mathbf{E}\right). \tag{3}$$

The subscripts e and i refer to electrons and ions, respectively. Equations (1) and (2) are the electron continuity and divergence-free current ($\mathbf{J}$) equations, respectively, while $\nu_{i,e}$ in equation (3) are the ion and electron's steady state velocities. The plasma is assumed to be charge neutral ($n_e = n_i = n$), and it is ensured by equation (2). The terms in the right-hand side of equation (1) correspond to the chemical loss of electrons by the charge exchange process (β) and the dissociative recombination (α) process. The notations $\kappa_{i,e}$ represent the ratios of the gyro frequencies, $\Omega_{i,e}$, to collision frequencies, $\nu_{i,en}$, of corresponding species; $b_{i,e} = e/m_{i,e}\nu_{i,en}$ represent the corresponding mobilities; $\mathbf{E}$ is the electric field in the neutral wind frame; $\hat{b}$ is the unit vector in the magnetic field (B) direction; and $c_{si,e}$ are the ions and electron thermal velocities, respectively. For further analysis, the thermal effects (i.e., diffusion effects) are neglected, restricting our investigation to be applicable only for large scales. The diffusion effects are important for studying the saturated turbulent state of the instability. However, in the present investigation the nonlinear evolution of the CII rather than the saturated turbulent state is investigated. With the valid E and F region approximation ($\kappa_e \gg 1$) the velocities then reduce to the following form:

$$\mathbf{v}_e = \frac{\kappa_e}{1 + \kappa_e^2}b_e\mathbf{E} \times \hat{b} \approx \frac{\mathbf{E}}{B} \times \hat{b} \tag{4}$$

$$\mathbf{v}_i = \frac{\kappa_i}{1 + \kappa_i^2}\left(\frac{\mathbf{g}}{\nu_{in}} + b_i\mathbf{E}\right) \times \hat{b} + \frac{1}{1 + \kappa_i^2}\left(\frac{\mathbf{g}}{\nu_{in}} + b_i\mathbf{E}\right). \tag{5}$$

We adopt the Cartesian coordinate system such that $\hat{x}$, $\hat{y}$, and $\hat{z}$ are along westward, upward, and northward directions. Since both E and F region instabilities are magnetic field-aligned instabilities, we model the equations in the plane perpendicular to B, that is, in the x-y plane. The substitution of the velocities in equation (2), with $\mathbf{E} = \mathbf{E}_o + \delta\mathbf{E}$, where $\mathbf{E}_o$ and $\delta\mathbf{E} = -\nabla\Phi$ are ambient and electrostatic perturbed fields, leads to the following equation for potential (Φ):

$$\frac{\partial^2\Phi}{\partial x^2} + \frac{\partial^2\Phi}{\partial y^2} + \frac{\partial \log n/\mu}{\partial x}\frac{\partial\Phi}{\partial x} + \frac{\partial \log n/\mu}{\partial y}\frac{\partial\Phi}{\partial y} - \mu\frac{\partial \log n}{\partial x}\frac{\partial\Phi}{\partial y}$$
$$+ \mu\frac{\partial \log n}{\partial y}\frac{\partial\Phi}{\partial x} = -B\left(\mu\kappa_i\frac{g}{\nu_{in}} - \frac{E_{xo}}{B} + \mu\frac{E_{yo}}{B}\right)\frac{\partial \log n}{\partial x}, \tag{6}$$

where $\mu = \psi\kappa_e/(1 - \psi)$, $\psi = 1/[\kappa_i(\kappa_e - \kappa_i)]$, and E_{xo} and E_{yo} represent the ambient westward and upward electric fields.

Since $\kappa_e \gg \kappa_i$ in both the E and the F regions, $\mu \approx 1/\kappa_i$, and then equation (6) can be written as

$$\nabla^2\Phi + \frac{\partial \log(\kappa_i n)}{\partial x}\frac{\partial\Phi}{\partial x} + \frac{\partial \log(\kappa_i n)}{\partial y}\frac{\partial\Phi}{\partial y} - \frac{1}{\kappa_i}\frac{\partial \log n}{\partial x}\frac{\partial\Phi}{\partial y}$$
$$+ \frac{1}{\kappa_i}\frac{\partial \log n}{\partial y}\frac{\partial\Phi}{\partial x} = -B\left(\frac{g}{\nu_{in}} - \frac{E_{xo}}{B} + \frac{1}{\kappa_i}\frac{E_{yo}}{B}\right)\frac{\partial \log n}{\partial x}. \tag{7}$$

This is the general two-dimensional (2-D) potential equation for both equatorial E and F region CII. We denote the term inside the parentheses of equation (7) as the source parameter, s, which can be rewritten as $s = g/\nu_{in} + v_{yo} + [(1/\kappa_i)v_{xo}]$, where v_{yo} and v_{xo} are the ambient upward and westward electron drift in the neutral wind frame obtained from equation (4). If the neutral wind is $\mathbf{w}$, then $s = g/\nu_{in} + v_{yo} - w_x [1/\kappa_i(w_y + v_{xo})]$, which is the same source term that appears in the growth rate expression (19) derived by *Basu* [2002] for general CII. Recently, *Keskinen et al.* [2003] have given a more general three-dimensional equation applicable for both the E and F regions. In the F region, where $\kappa_i \gg 1$, all the terms appearing with factor $1/\kappa_i$ in equation (7) are negligible, and then equation (7) is identical to the potential equation used by *Sekar et al.* [1994] for GRT in the F region. The electron continuity equation (1) can now be written as

$$\frac{\partial n}{\partial t} + \mathbf{\nabla} \cdot \left(n\frac{(\mathbf{v_o} - \nabla\Phi) \times \hat{\mathbf{b}}}{B}\right) = -\beta n - \alpha n^2$$

or

$$\frac{\partial n}{\partial t} + \nabla \cdot \mathbf{F} = -R_e n, \tag{8}$$

where

$$R_e = \left[\frac{1}{\beta} + \frac{1}{\alpha n(t)}\right]^{-1}$$

is the effective recombination rate and

$$\mathbf{F} = \boldsymbol{n}\frac{(\mathbf{v_o} - \nabla\Phi) \times \hat{\mathbf{b}}}{\mathbf{B}} = \boldsymbol{n}\mathbf{V}$$

is the particle flux. In the flux form the electrostatic condition $\nabla \times \mathbf{E} = \mathbf{0}$ reduces to the form

$$\nabla \cdot \mathbf{F} = \mathbf{F} \cdot \nabla \log \boldsymbol{n},$$

and thus the continuity equation can be written as

$$\frac{\partial n}{\partial t} + \mathbf{F} \cdot \nabla \log \boldsymbol{n} = -\boldsymbol{R_e n}. \tag{9}$$

Equations (7) and (9) form the coupled closed system of equations for CII in the E and F regions. The potential equation is solved, at first, by a successive overrelaxation algorithm with chosen initial density perturbation. The
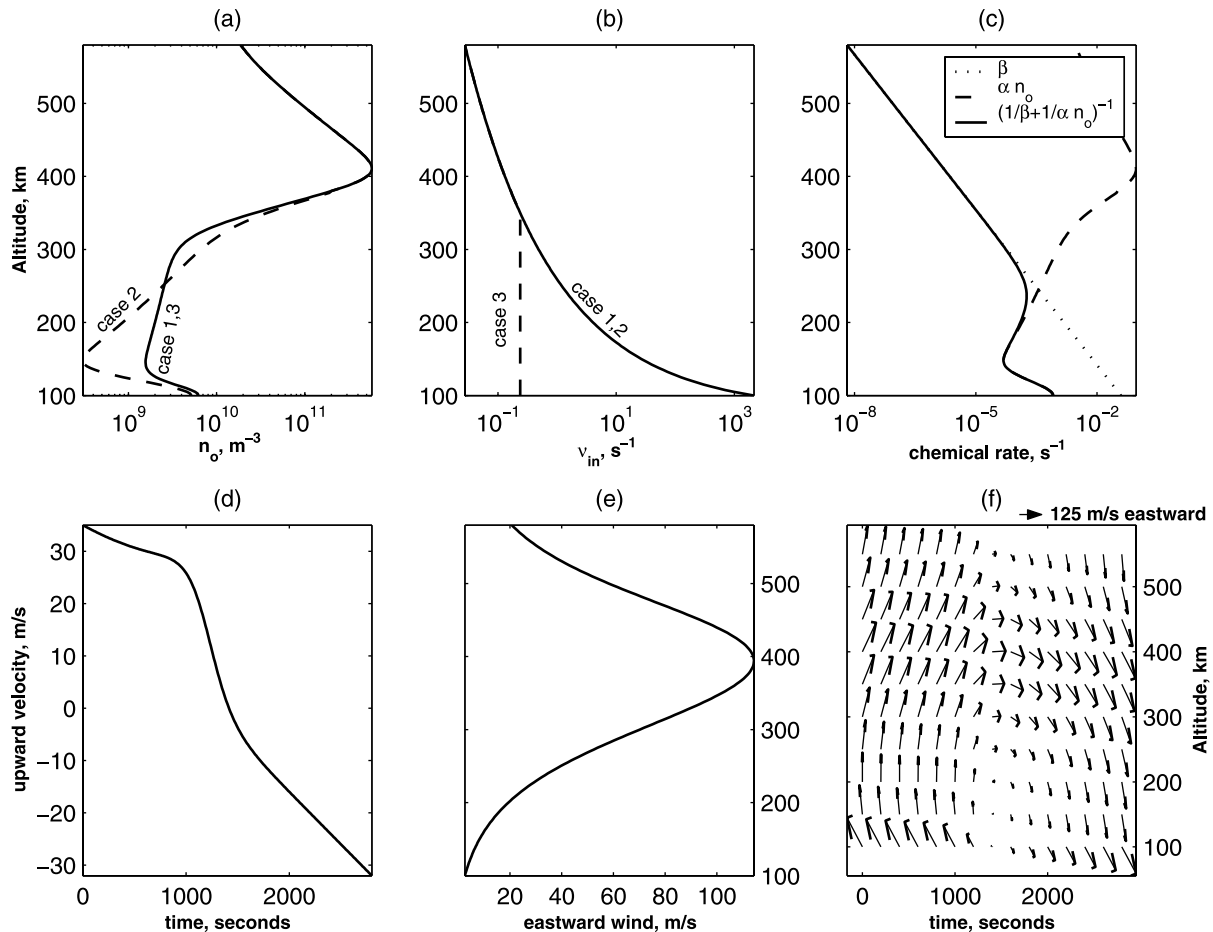
Figure 1. (a) Altitude versus n_o, (b) altitude versus ν_{in}, (c) altitude versus reaction rates, (d) vertical velocity versus time, (e) altitude versus eastward wind, and (f) velocity vector over altitude-time plane.

Crank-Nicholson implicit scheme is then applied for the time integration of continuity equation (9).

3. Results and Discussion

[6] The purpose of the present investigation is to examine the effects of GRT on the valley (150–200 km) and upper E (110–130 km) regions. For this we have chosen 100 and 500 km as the lower and upper boundaries, respectively, of the simulation. The transmittive boundary condition on n and the Neumann boundary condition on Φ are imposed. These boundary conditions are the same as those chosen by *Sekar et al.* [1994] and are sufficient to ensure the vanishing current density across the lower boundary provided ambient ionosphere is invariant at the boundary. In Figure 1, various profiles of electron number density, n_o (Figure 1a), and ν_{in} (Figure 1b) are plotted. The different profiles correspond to different cases described later. Unless mentioned, the results described below correspond to the profiles plotted as case 1 in Figure 1. The profiles in case 1 are similar to the profiles given by *Kelley* [1989] and *Zalesak et al.* [1982]. In Figure 1c the effective recombination rate is plotted. It is clear that the effective recombination rate follows dissociative recombination in the E region and the charge exchange rate in the F region. The vertical velocity profile is chosen similar to the model evening hour profile of

Haerendel et al. [1992] and is plotted in Figure 1d. We follow expression (18) of *Çakir et al.* [1992] to calculate the zonal velocity from the vertical velocity profile and zonal wind. Though the exact calculation requires field-aligned integrated quantities, the local quantities with adjusting weighing factors should be adequate qualitatively. In terms of local quantities the zonal velocity can be written as

$$v_{xo} = f_1 \frac{\nu_{in}}{\Omega_i} v_{yo} + f_2 w_{xo},$$

where w_{xo} is the zonal wind taken to be time independent, and is plotted in Figure 1e. Though the vertical velocity varies with altitude [*Fejer et al.*, 1996] because of the time-dependent wind, the altitude-independent vertical velocity profile is a fair approximation so far as the evolution of the instability is concerned. However, for a realistic model one should take the proper time-dependent wind and altitude-dependent vertical velocity profile. In Figure 1f the velocity vector $\mathbf{V_o} = -\mathbf{v_{xo}}\hat{\mathbf{x}} + \mathbf{v_{yo}}\hat{\mathbf{y}}$ is plotted by adjusting the factors f_1 and f_2 in the expression of v_{xo}, such that the profile becomes similar to the profile given by *Haerendel et al.* [1992] and observed by *Kudeki and Bhattacharyya* [1999].

[7] The initial sinusoidal density perturbation is assumed in the zonal direction with 5% amplitude and 100 km wavelength. Moreover, only the valley and bottomside F
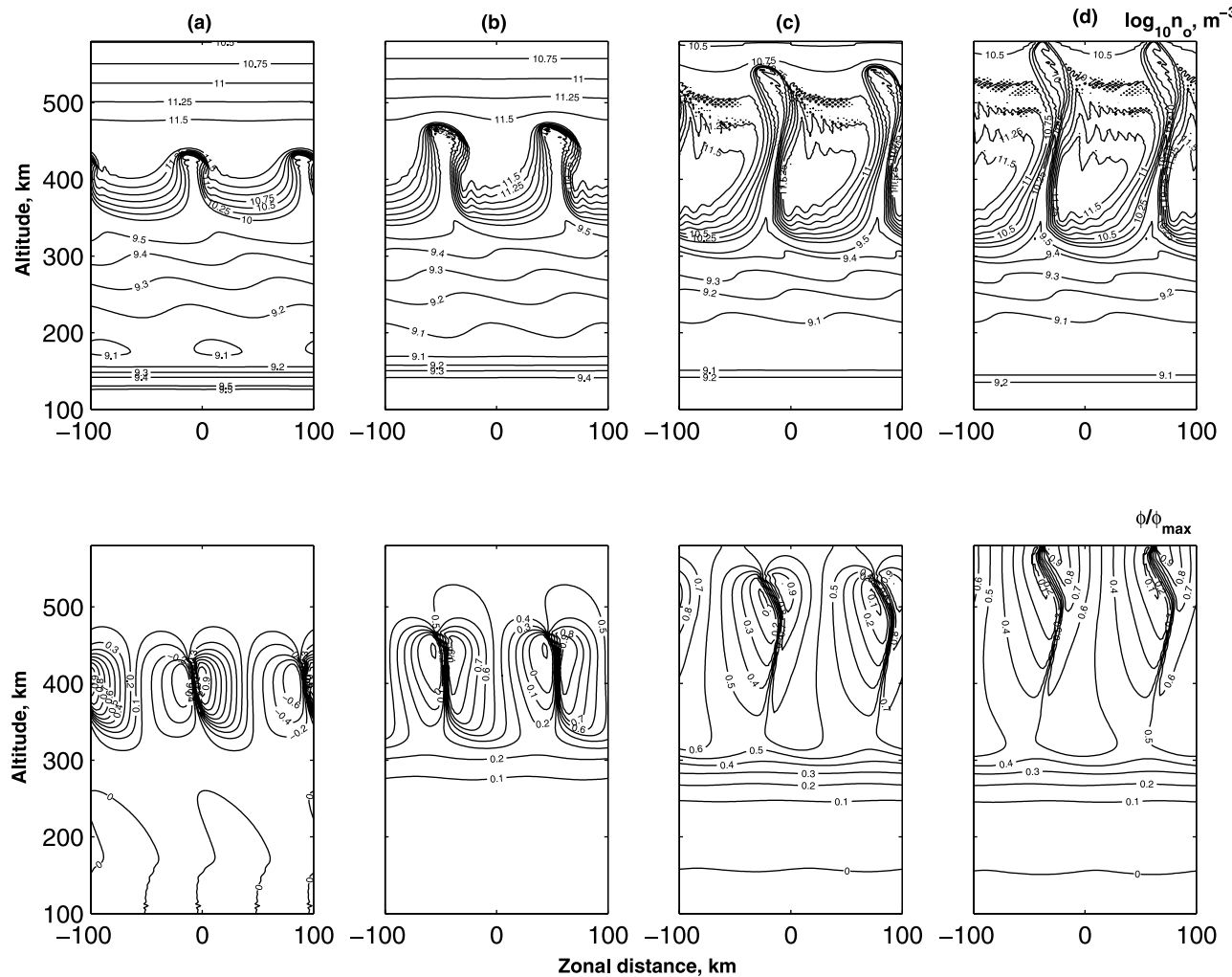
Figure 2. Contours of (top) $\log_{10} n$ and (bottom) normalized potential (ϕ/ϕ_{max}) at (a) 1000, (b) 1400, (c) 1800, and (d) 2200 s.

regions are subjected to the initial perturbation. In the top (bottom) plots of Figures 2a–2d, the isodensity (isopotential) contours are plotted over the simulation plane at 1000, 1400, 1800, and 2200 s, respectively. The evolution of isodensity contours (IDCs) as the bubble structures is evident. The evolution characteristics are similar to the characteristics described by earlier simulations [*Zalesak et al.*, 1982; *Sekar et al.*, 1994]. The bottom plots, in addition, reveal that as time progresses, the potential contours tend to be confined near the altitude region of large density gradient. Such a characteristic of the fringe field was noted and explained by *Zalesak and Ossakow* [1980]. Thus the present model efficiently describes the nonlinear evolution of GRT over large scales.

[8] In order to investigate the fringe field effects beneath the F region, the wavelength of zonal perturbation is increased from 100 to 500 km since the large wavelengths are expected to penetrate deep beneath the F region [*Zalesak and Ossakow*, 1980]. Moreover, the degree of penetration is also expected to depend on the ambient conductivity profile which is essentially dictated by the density and collision frequency profiles. Depending on the various density and collision frequency profiles, the

following cases are considered: case 1, the profiles of $n_o(y)$ and ν_{in} as plotted in Figure 1; case 2, all profiles the same as in case 1 except $n_o(y)$, which is altered and plotted in Figure 1a; case 3, all profiles the same as in case 1 except ν_{in}, which is altered such that $\nu_{in(y<380km)} = \nu_{in(y=380km)}$ and is plotted in Figure 1b.

[9] The contours in Figures 3a and 4a represent the IDCs over 100–580 and 100–300 km altitude regions, respectively, under case 1. The results correspond to the time $t = 2400$ s. For comparison, the IDCs at $t = 0$ s and over 100–300 km are plotted in Figure 4d. The development of the bubble is evident from Figure 3a. It is further evident from Figure 4a that the contours in the valley and upper E regions are not evolved with time, though the bubble has fully developed in the F region. The unevolved contours or insignificant modulation of contours in the valley and E regions indicate the insignificant transport of plasma in these regions. We have also found that the potential contours corresponding to Figure 3a do penetrate beneath the F region. However, they are very low potential contours separated far apart zonally and are unable to give rise to any significant transport of the plasma in the region. Thus the fringe field generated by the GRT does penetrate
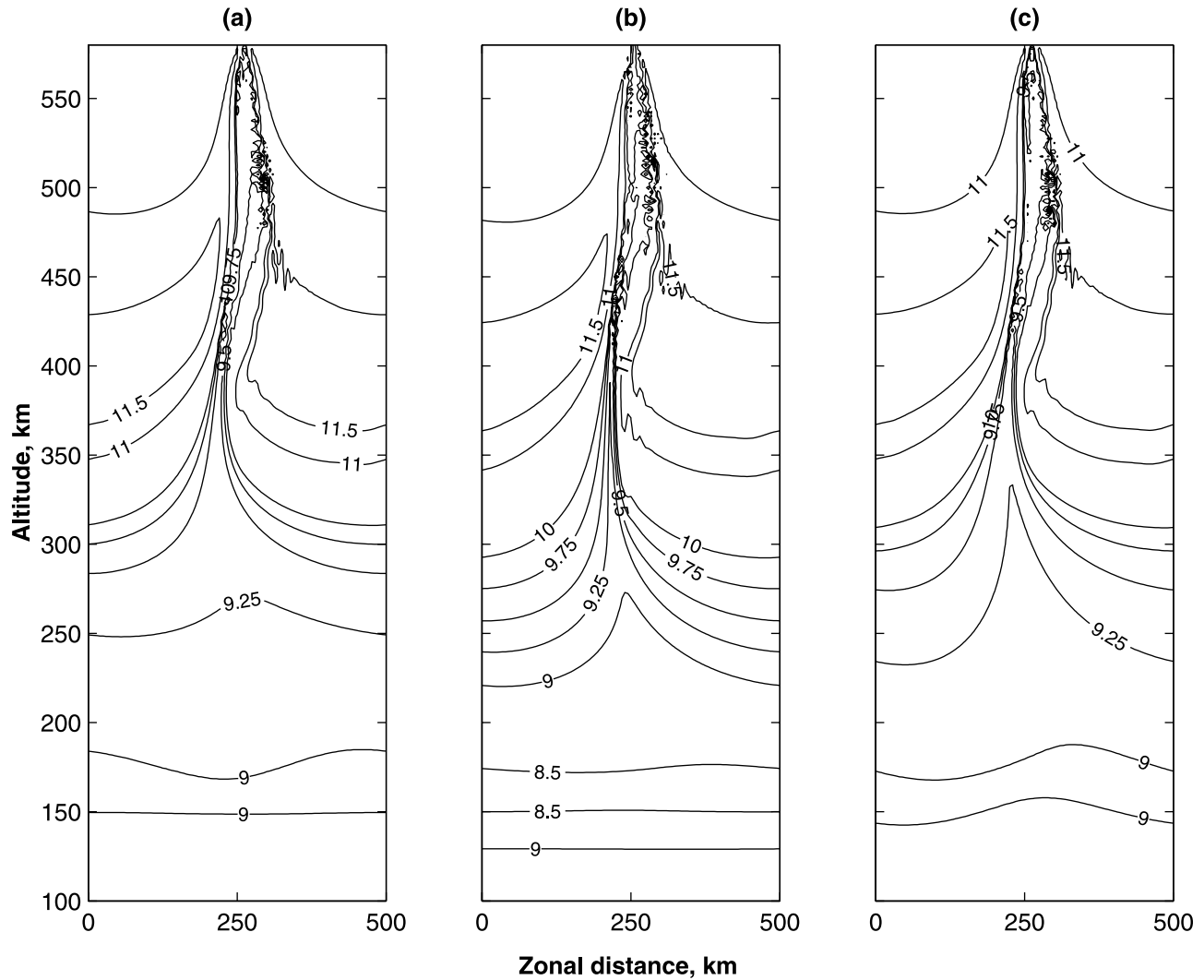
Figure 3. Contours of $\log_{10} n$ ($t = 2400$ s) over $100-580$ km for (a) case 1, (b) case 2, and (c) case 3.

beneath the *F* region, but it is incapable of transporting the plasma to higher altitudes under case 1.

[10] *Zalesak and Ossakow* [1980] have investigated the characteristics of the fringe field at length. They have found that during the nonlinear evolution of GRT the fringe field tends to confine toward the large density gradient in the *F* region. Such characteristics thus reveal that the degree of penetration of the fringe field depends on the density profile beneath the *F* region. In order to investigate such effect in detail, we have run the simulation under case 2. Unlike case 1, the density profile for case 2 is chosen such that the density gradient in the $200-300$ km region remains large. The contours shown in Figures 3b and 4b represent the evolution of IDCs under case 2 in $100-580$ and $100-300$ km altitude regions, respectively, at $t = 2400$ s. The similar evolution characteristic of bubbles under cases 1 and 2 is evident from Figures 3a and 3b. However, the IDCs lying below 250 km altitude are modulated to the large amplitude under case 2 as compared with their insignificant modulations under case 1. These enhanced modulations represent the enhanced transport of plasma in this region. They also indicate that the stronger fringe field has penetrated beneath the *F* region under case 2 as compared with case 1.

[11] The numerical simulation of GRT reveals that during the nonlinear evolution the bubble penetrates beyond F_{peak} and continues to rise on the topside. It means that the fringe field extends beyond F_{peak} in spite of the negative gradient on the topside. On the other hand, investigation under case 2 reveals that the penetration of the fringe field down beneath the *F* region requires significant positive density gradient. The opposite behavior of the fringe field on the topside and beneath the *F* region indicates that apart from density gradient, other ambient quantities should also play the decisive role for the extension and penetration of the fringe field. The ambient quantities which can be important in this context are ν_{in} or κ_i because their behaviors are drastically different on the topside and beneath the *F* region. Moreover, together with the density profile, the profile of κ_i decides the conductivity profiles, which is crucial for the generation of any electric field in the ionosphere. In order to confirm our argument, we have investigated the effect of ν_{in} on the penetration of the fringe field under case 3. The contours depicted in Figures 3c and 4c represent the evolution of IDCs in $100-580$ and $100-300$ km altitude regions, respectively, under case 3. The bubble evolution characteristic of case 3 is similar to that of cases 1 and 2. However,
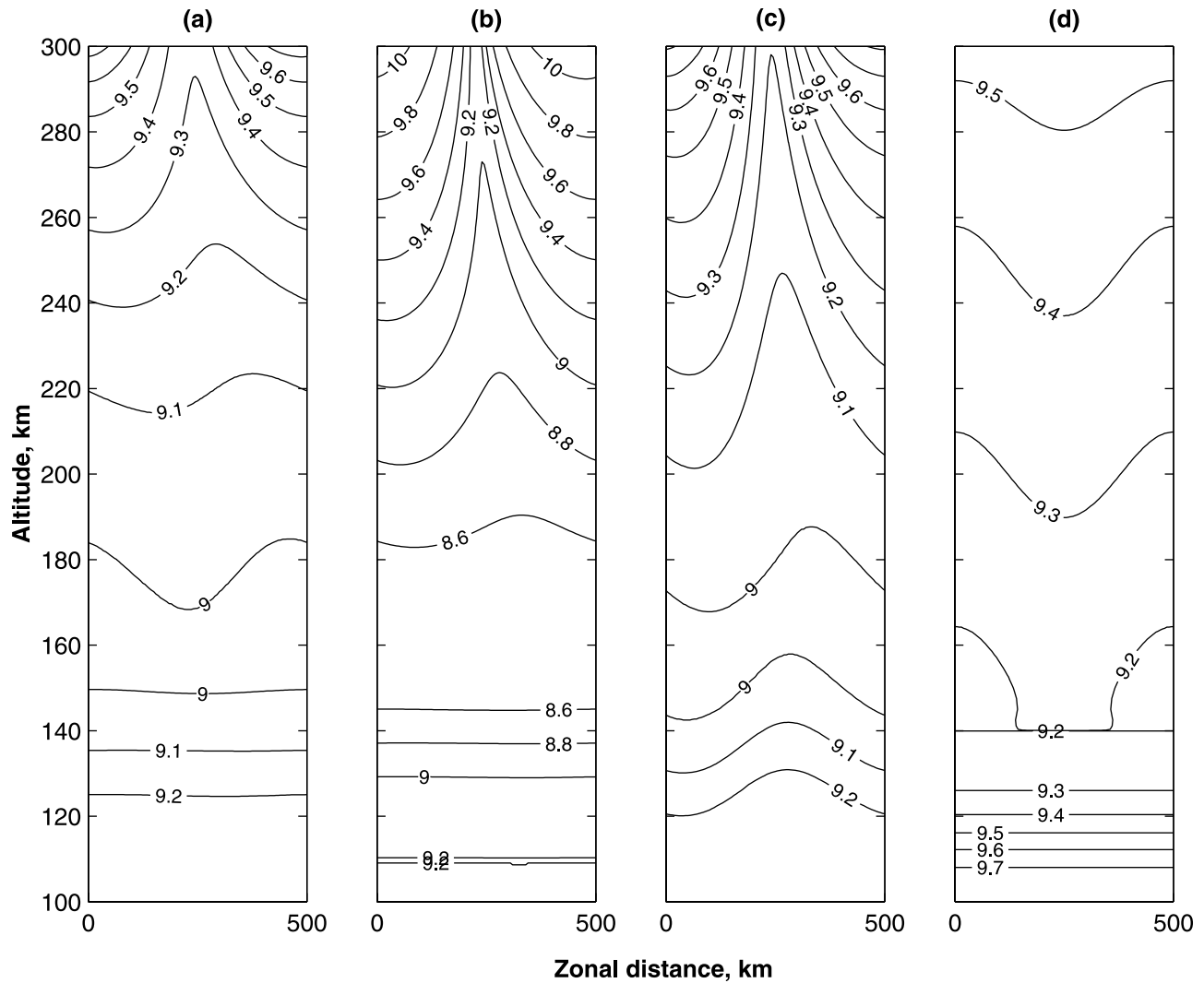
Figure 4. Contours of $\log_{10} n$ ($t = 2400$ s) over $100-300$ km for (a) case 1, (b) case 2, and (c) case 3 and (d) contours of $\log_{10} n$ ($t = 0$ s) over $100-300$ km.

unlike case 1, IDCs lying below 250 km are modulated to large amplitude in case 3, thus indicating the significant transport of plasma in this region. Thus, similar to case 2, the stronger fringe field has penetrated into the valley region under case 3. Moreover, unlike case 2, modulations of IDCs in the *E* region are also evident in case 3. Thus the fringe field has further penetrated into the *E* region in case 3 as compared with its insignificant penetration in case 2. These characteristics reveal that the effect of ν_{in} on the fringe field is as crucial as the density gradient. The physical reason for the penetration of a stronger fringe field under case 3 as compared with case 1 can be argued as follows: It is known that the polarization field generated by the GRT in the *F* region is Pedersen in nature because both ions and electrons are magnetized, and thus the main contribution in current comes from Pedersen conductivity instead of Hall conductivity. On the other hand, the dominant field generated in the *E* region is Hall in nature. The transition from Pedersen to Hall nature of the field arises because of the change in the ratio $\kappa_i = \Omega_i/\nu_{in}$, which is much smaller (larger) than unity in the equatorial *E* (*F*) region. By assuming $\nu_{in(y<380)} = \nu_{in(y=380)}$ in case 3, we have, in fact, made the conductivity

Pedersen in nature throughout in the valley and upper *E* region. In turn, it supports the polarization field of GRT to penetrate beneath the *F* region in contrast with case 1, where Hall conductivity dominates toward the *E* region.

[12] The investigations under cases 2 and 3 reveal that the conductivity profiles play a decisive role for the significant penetration of a stronger fringe field beneath the *F* region. It should be noted that in spite of the very small density gradient in the valley region and the negative gradient in the upper *E* region the strong fringe field has penetrated down to the *E* region under case 3. Thus, regardless of the density gradient, the fringe field can penetrate significantly into the region where the ratio κ_i remains large, that is, where ions are magnetized. We therefore expect the stronger fringe field to penetrate in the valley region and up to the upper boundary of the *E* region where κ_i is not very large but still remains much larger than unity. Even within the *E* region, where κ_i is of the order of unity or not much less than unity, we expect the fringe field to remain effectively strong. On the other hand, we do not expect the fringe field to remain stronger in the region where κ_i is much smaller than unity, that is, where ions are highly unmagnetized.
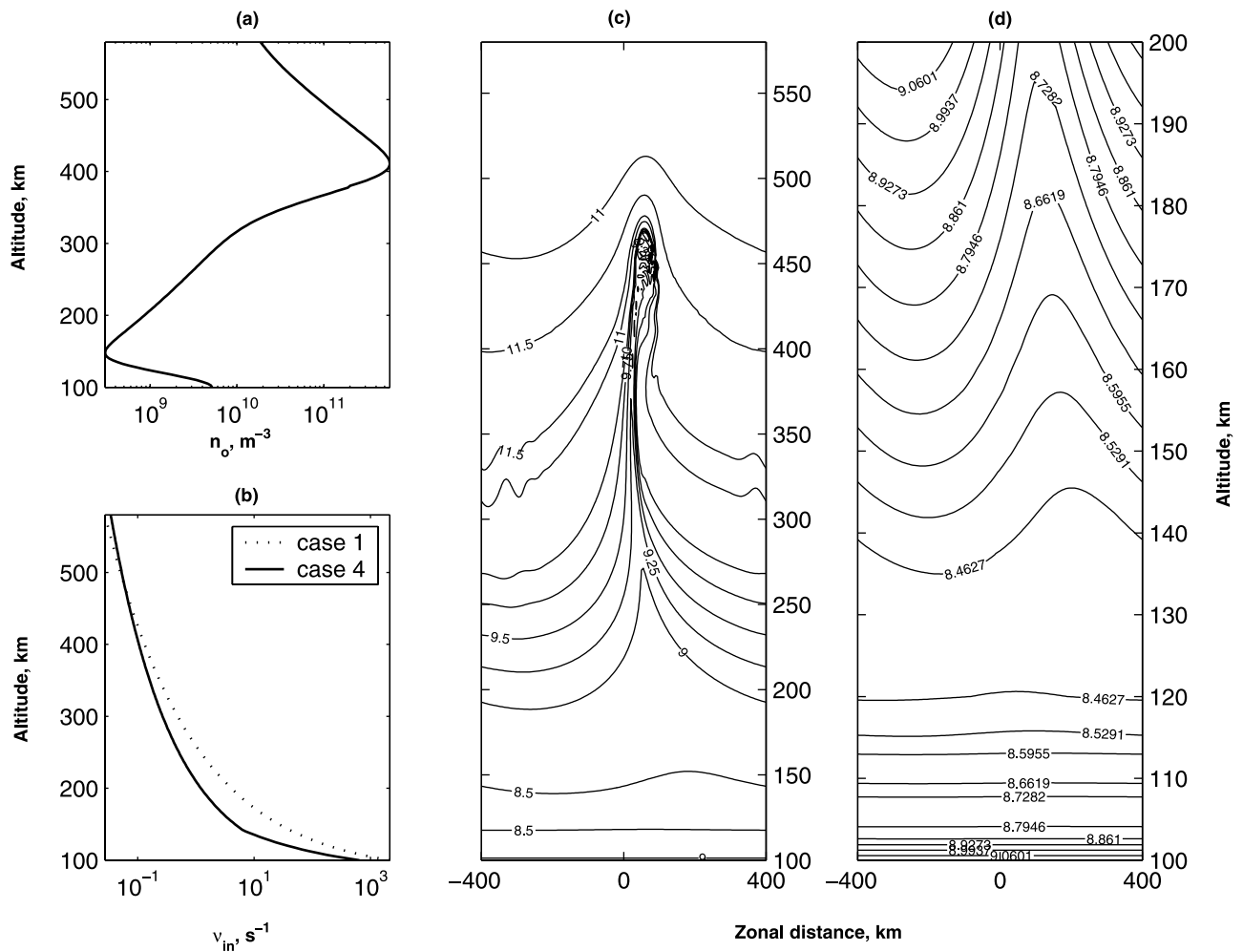
Figure 5. Altitude profiles of (a) density and (b) ν_{in} and contours of $\log_{10} n$ ($t = 3200$ s) over (c) 100–580 km and (d) 100–200 km for case 4.

[13] The profile of ν_{in} in case 3 is not realistic, but the profile of n_o in case 2 can be realized under a quiet ionosphere. Moreover, it is possible to achieve a realistic profile of ν_{in} which is intermediate to the profiles assumed in cases 1 and 3. Together with the density profile assumed under case 2, such an intermediate profile of ν_{in} can give rise to the suitable conductivity profiles which allow the stronger fringe field to penetrate significantly beneath the F region. We would like to point out that the present simulation is confined in the plane perpendicular to the magnetic field where local ambient ionospheric profiles are considered. In order to have an exact description of the dynamics beneath the F region, a 3-D simulation or flux tube-integrated profiles are desired. Flux tube–integrated conductivity profiles look quite different from local profiles, and the variations in the integrated conductivities with decreasing altitude are rather more gradual [*Haerendel et al.*, 1992]. Thus it is likely that under the flux tube-integrated consideration the intermediate ν_{in} profile and thus the suitable and realistic conductivity profiles can be achieved. We would now like to present one such case where an intermediate ν_{in} profile is considered. This case is referred to as case 4, and the corresponding inputs and results are plotted in Figure 5. The density profile is plotted in Figure 5a, and it is identical to the profile considered under case 2. The intermediate ν_{in} profile is plotted in Figure 5b. For comparison, the ν_{in} profile under case 1 is also plotted. The wavelength of initial perturbation is also increased to 800 km for the present case. The contours of $\log_{10} n$ are plotted over 100–580 and 100–200 km in Figures 5c and 5d, respectively. The significant modulations of IDCs lying below 200 km are noted in Figure 5d during the developed phase of the bubble. The contours lying in the upper E region are extended to the valley region while contours lying in the valley region are extended to the F region. This means that the plasma is transported from the E region to the valley region and even farther to the F region. In Figure 5d, slight modulation is seen near 120 km, though this region was not perturbed initially. This means that the fringe field is capable of recognizing the plasma within the E region. If this region (near 120 km) is perturbed initially, we expect significant modulation in this region also. In this region, ions are marginally magnetized. This means that the fringe field can remain effectively stronger in the region where ions are marginally magnetized. It should also be noted that case 4 represents the strongly driven condition where ions remain marginally magnetized up to 120 km. Thus the fringe field of GRT can transport the plasma from that part of the E region to the valley and F regions only under strongly driven conditions.

[14] Apart from the conductivity profile being a primary cause, there are secondary causes that can affect the degree of penetration of the fringe field. One of them is the shear in the zonal plasma drift, which is highly variable in nature. We have found that the reduction in the shear in the zonal plasma drift in the $100-300$ km altitude region supports the penetration of a stronger fringe field.

[15] In earlier investigations [*Zalesak and Ossakow*, 1980; *Alam Kherani et al.*, 2002] the characteristics of the fringe field beneath the *F* region were described qualitatively without considering the dynamics of the region. In contrast, the present investigation quantitatively describes the characteristics of the fringe field beneath the *F* region. The degree of penetration of the fringe field and its magnitude are determined under different conductivity profiles beneath the *F* region. The importance of the ratio κ_i in determining the magnitude and penetration of the fringe field is investigated for the first time. In our earlier qualitative investigation we had argued that the fringe field is capable of transporting the irregularities from the deep *E* region. In the present investigation we have quantified such description and have examined the suitable conditions for the penetration of a stronger fringe field into the *E* region.

[16] The aforementioned characteristics of the fringe field become crucial in the context of valley region echoes observed by VHF radar [*Woodman and La Hoz*, 1976; *Hysell et al.*, 1990; *Woodman and Chau*, 2001]. These observations reveal the presence of irregular structures originating from the *E* region and merging into the plume in the *F* region. It is generally believed that the echoes observed in the $120-200$ km altitude region are caused by the convection of *E* region irregularities under the action of the fringe field [*Alam Kherani et al.*, 2002]. The investigation under case 4 reveals that the strong fringe field can recognize and transport the part of the *E* region plasma lying near and above 120 km. However, it is not possible for the fringe field to remain stronger deeper (below $120-115$ km) into the *E* region where ions are highly unmagnetized. During nighttime the *E* region irregularities are usually located at $100-125$ km altitude, which covers both highly ion-unmagnetized and marginally ion-magnetized regions [*Fejer et al.*, 1975]. Since the fringe field is capable of recognizing the plasma down to the marginally ion-magnetized region, we expect the strong interaction between *E* region irregularities and the fringe field. Since the fringe field is eastward, such interaction can lead to the convection of *E* region irregularities to the higher altitude and even across the valley region up to the lower boundary of the *F* region. Such a mechanism thus can cause the valley region echoes observed by radar. Moreover, the radar observation [*Woodman and Chau*, 2001] shows that the irregularities lying near 120 km are convected to the higher altitude. The irregularities lying below this altitude remain in the *E* region. As the fringe field is effective only in the part of the *E* region near and above 120 km, our quantitative description seems to be consistent with such observational characteristics.

4. Summary and Conclusions

[17] The implicit code is implemented for the collisional interchange instability in the equatorial *E* and *F* regions.

The effects of the fringe field into the valley and *E* regions are examined under different ambient ionospheric conditions. We found that the conductivity profiles beneath the *F* region play a decisive role in the significant penetration of the fringe field. Only suitable conductivity profiles, under strongly driven conditions, allow the stronger fringe field to penetrate down to the *E* region. We have shown that the fringe field is the effective mechanism of transport of plasma throughout the strongly ion-magnetized region. We have further shown that under strongly driven conditions, the fringe field is capable of recognizing and transporting the *E* region plasma where ions are marginally magnetized (near and above 120 km). The part of the *E* region type-II irregularities are often located in such a region during evening and nighttime. These irregularities can be effectively transported across the valley region by the eastward fringe field to give rise to the frequently observed valley region echoes. On the other hand, the fringe field is incapable of transporting the *E* region plasma lying in the highly ion-unmagnetized region, that is, beneath $120-115$ km altitude. The *E* region irregularities located in this region are not influenced by the fringe field.

References

Alam Kherani, E., R. Sekar, and R. Raghavarao (2002), Equatorial rising structure in night-time *E* region: A manifestation of electro dynamical coupling of spread *F*, *J. Atmos. Sol. Terr. Phys.*, *64*, 1505.

Basu, B. (2002), On the linear theory of equatorial plasma instability: Comparison of different descriptions, *J. Geophys. Res.*, *107*(A8), 1199, doi:10.1029/2001JA000317.

Çakir, S., G. Haerendel, and J. V. Eccles (1992), Modeling the ionospheric response to artificially produced density enhancements, *J. Geophys. Res.*, *97*, 1193.

Fejer, B. G., D. T. Farley, B. B. Balsley, and R. F. Woodman (1975), Vertical structure of the VHF backscattering region in the equatorial electrojet and the gradient drift instability, *J. Geophys. Res.*, *80*, 1313.

Fejer, B. G., E. R. de Paula, L. Scherliess, and I. S. Batista (1996), Incoherent scatter radar, ionosonde and satellite measurements of equatorial *F* region vertical plasma drifts in the evening sector, *Geophys. Res. Lett.*, *23*, 1733.

Haerendel, G. (1973), Theory of equatorial spread *F*, unpublished report, Max-Plank Inst. für Phys. und Astrophys., Garching, Germany.

Haerendel, G., J. V. Eccles, and S. Çakir (1992), Theory for modeling of the equatorial evening ionosphere and the origin of the shear in the horizontal plasma flow, *J. Geophys. Res.*, *97*, 1209.

Huang, C. S., M. C. Kelley, and D. L. Hysell (1993), Nonlinear Rayleigh-Taylor instabilities, atmospheric gravity waves, and equatorial spread *F*, *J. Geophys. Res.*, *98*, 15,631.

Huba, J. D., G. Joyce, and J. A. Fedder (2000), Sami2 is Another Model of the Ionosphere (SAMI2): A new low-latitude ionosphere model, *J. Geophys. Res.*, *105*, 23,035.

Hysell, D. L., M. C. Kelley, W. E. Swartz, and R. F. Woodman (1990), Seeding and layering of equatorial spread *F* by gravity waves, *J. Geophys. Res.*, *95*, 17,253.

Kelley, M. C. (1989), *The Earth's Ionosphere*, Elsevier, New York.

Kelley, M. C., M. F. Larsen, C. La Hoz, and J. P. McClure (1981), Gravity wave initiation of equatorial spread *F*: A case study, *J. Geophys. Res.*, *86*, 9087.

Keskinen, M. J., S. L. Ossakow, and B. G. Fejer (2003), Three-dimensional nonlinear evolution of equatorial ionospheric spread-*F* bubbles, *Geophys. Res. Lett.*, *30*(16), 1855, doi:10.1029/2003GL017418.

Kudeki, E., and S. Bhattacharyya (1999), Postsunset vortex in equatorial *F*-region plasma drifts and implications for bottomside spread-*F*, *J. Geophys. Res.*, *104*, 28,163.

Ossakow, S. L., S. T. Zalesak, B. E. McDonald, and P. K. Chaturvedi (1979), Nonlinear equatorial spread *F*: Dependence on altitude of the *F* peak and bottom-side background electron density gradient scale length, *J. Geophys. Res.*, *84*, 17.

Raghavarao, R., R. Sekar, and R. Suhasini (1992), Nonlinear numerical simulation of equatorial spread *F*—Effects of winds and electric fields, *Adv. Space Res.*, *12*, 227.

Scannapieco, A. J., and S. L. Ossakow (1976), Nonlinear equatorial spread *F*, *Geophys. Res. Lett.*, *3*, 451.

Sekar, R., R. Suhasini, and R. Raghavarao (1994), Effects of vertical winds and electric fields in the nonlinear evolution of equatorial spread *F*, *J. Geophys. Res.*, *99*, 2205.

Woodman, R. F., and J. L. Chau (2001), Equatorial quasiperiodic echoes from field-aligned irregularities over Jicamarca, *Geophys. Res. Lett.*, *28*, 207.

Woodman, R. F., and C. La Hoz (1976), Radar observations of *F* region equatorial irregularities, *J. Geophys. Res.*, *81*, 5447.

Zalesak, S. T. (1979), Fully multidimensional flux-corrected transport algorithms for fluids, *J. Comput. Phys.*, *31*, 335.

Zalesak, S. T., and S. L. Ossakow (1980), Nonlinear equatorial spread *F*: Spatially large bubbles resulting from large horizontal scale initial perturbations, *J. Geophys. Res.*, *85*, 2131.

Zalesak, S. T., S. L. Ossakow, and P. K. Chaturvedi (1982), Non-linear equatorial spread *F*: The effect of neutral winds and background Pedersen conductivity, *J. Geophys. Res.*, *87*, 151.

Zargham, S., and C. E. Seyler (1987), Collisional interchange instability: Numerical simulations of intermediate-scale irregularities, *J. Geophys. Res.*, *92*, 10,073.

————————————

E. Alam Kherani, F. C. P. Bertoni, and E. R. de Paula, INPE, São José dos Campos, São Paulo, Brasil. (alam@dae.inpe.br)